Journal of Energy Storage 162 (2026) 122082

Contents lists available at ScienceDirect

Journal of Energy Storage

journal homepage: www.elsevier.com/locate/est

Research papers

Early hydrogen gas detection as a predictive strategy for thermal runaway mitigation in lithium-ion batteries under variable heating conditions

Sanghyun Park [a,1], Mingi Kim [b,1], Je-seong Oh [c,1], Minuk Kim [d,1], Kyung-Ho Park [b], Kwang-young Yoo [b], Min-Jae Kim [a], Keunhyung Lee [a,e], Mi-Sung Kim [e], Hyun-Sook Lee [a,*], Jongsup Hong [b,c,d,**], Wooyoung Lee [a,b,*]

[a] Department of Material Science and Engineering, Yonsei University, Seoul 03722, Republic of Korea
[b] Department of Battery Engineering, Yonsei University, Seoul 03722, Republic of Korea
[c] Department of Battery Conflation Engineering, Yonsei University, Seoul 03722, Republic of Korea
[d] Department of Mechanical Engineering, Yonsei University, Seoul 03722, Republic of Korea
[e] Korea Testing & Research Institute, 98, Gyoyugwon-ro, Gwacheon-si, 13810, South Korea

ARTICLE INFO

Keywords:
Lithium-ion batteries
Thermal runaway
Hydrogen gas sensing
Early warning
Battery safety

ABSTRACT

Thermal runaway (TR) is one of the most critical safety concerns in lithium-ion batteries (LIBs), particularly under abusive thermal conditions. Among early-stage TR indicators, H_2 evolution has emerged as a chemically specific and temporally leading signal. Compared with conventional monitoring approaches relying primarily on temperature or pressure signals, hydrogen evolution provides a chemically specific indicator of early degradation processes preceding TR. However, quantitative frameworks linking H_2 generation with TR onset under realistic heating conditions remain limited. Herein, a Pd-decorated SnO_2 nanorod sensor capable of real-time H_2 detection at ppm levels is used to examine the TR behavior of a model LIB at heating rates of 5, 7, 10, and 15 °C/min. H_2 evolution is shown to start at ~100 °C, i.e., well before TR initiation (>180 °C), and a practical onset criterion (~10 ppm) enables early warnings preceding TR by 5–24 min (Δt_{TR}), depending on the heating rate. To quantitatively characterize the warning behavior beyond onset timing, key indicators including t_{H2} (first H_2 detection time), Δt_{TR}, $[H_2]_{peak}$ (peak concentration), and the peak of $d[H_2]/dt$ are analyzed. Notably, $[H_2]_{peak}$ and $d[H_2]/dt$ exhibit heating-rate-dependent nonlinear changes under accelerated heating, consistent with a reduced mitigation window. In situ mass spectrometric analysis confirms the presence of H_2 in the evolved gases, supporting its role as a reliable TR precursor. Beyond simple gas detection, we further introduce a two-stage, time-resolved warning framework in which early-stage indicators (H_2 onset and cell surface temperature) are combined with imminent pre-TR indicators characterized by a rapid rise and peak in $d[H_2]/dt$, enabling discrimination between off-gassing and critical transition regimes preceding thermal runaway.

1. Introduction

Lithium-ion batteries (LIBs) are at the core of today's electrification landscape, finding applications ranging from mobile devices and electric vehicles to grid-scale energy storage systems [1–5]. The high energy density, long cycle life, and minimal self-discharge of LIBs make them the preferred choice in numerous industries [6,7]. However, LIBs pose the risk of thermal runaway (TR), an uncontrollable exothermic reaction that can cause rapid heating, gas release, and ultimately fire or explosion. The recent high-profile incidents involving electric-vehicle fires and energy storage system explosions indicate that ensuring LIB safety is no longer optional but essential for its widespread deployment in the energy market [8–10].

Given the importance of early TR detection for preventing catastrophic failure, several corresponding approaches have been proposed, primarily relying on temperature, pressure, and electrochemical (e.g., EIS) diagnostics [11–13]. Each of the examined approaches has shown potential, but none has achieved the sensitivity, specificity, and response

* Corresponding authors at: Department of Materials Science and Engineering, Younsei University, Seoul 03722, Republic of Korea.
** Correspondence to: J.S. Hong, Department of Mechanical Engineering, Younsei University, Seoul 03722, Republic of Korea.
E-mail addresses: h-slee@yonsei.ac.kr (H.-S. Lee), jongsup.hong@yonsei.ac.kr (J. Hong), wooyoung@yonsei.ac.kr (W. Lee).
[1] These authors contributed equally to this work.

https://doi.org/10.1016/j.est.2026.122082
Received 31 December 2025; Received in revised form 6 March 2026; Accepted 2 April 2026
Available online 8 April 2026
2352-152X/

time required for reliable real-world deployment. Temperature sensors, although widely used, often do not exhibit timely responses because of thermal delays between the cell core and surface [14–16]. Pressure sensors, while useful for capturing internal gas buildup, cannot discriminate between gas types or identify the reaction stage [17,18]. Electrochemical impedance spectroscopy can detect chemical changes but requires cells to be idle and produces difficult-to-interpret signals [19–21]. Thus, all of these three techniques are limited in their ability to accurately predict the onset of TR in real time.

Alternatively, gas (especially H_2) sensing is a promising early-TR-detection techniques, as H_2 is one of the gases released earliest prior to TR and is often generated through solid–electrolyte interphase (SEI) breakdown, lithium dendrite–binder reactions, and early electrolyte decomposition. Owing to its high diffusion rate, low ignition threshold (~4 vol%), and distinct chemical signature, H_2 is easily detected and ideally suited for the early-stage monitoring of battery instability [22–26].

Recent advances in sensing have enabled the development of platforms capable of detecting H_2 as one of the earliest indicators of battery degradation during the onset of TR [25,27–29]. These platforms include metal-oxide semiconductor sensors relying on surface reaction–induced conductivity changes [30], optical sensors exploiting light–gas interactions [31], and field-effect transistor (FET)–based architectures designed for low-concentration detection [32,33]. Despite featuring different operating principles, these platforms share a common goal, namely rapid, selective, and reliable H_2 detection in complex battery environments. However, the practical deployment of H_2 sensing for early TR detection remains limited for the following reasons.

- Existing studies generally employ fixed heating rates, ignoring the impact of different TR induction conditions. Real-world scenarios include internal short-circuiting, mechanical abuse, and external heating and may result in broadly variable heating rates (5–15 °C/min), which can dramatically affect the timing and extent of gas release. If this possibility is not accounted for, the practical predictability of H_2 detection remains uncertain.
- Previous studies focus on whether H_2 is detected or not, with few considering how early it is detected or how the detection window narrows or widens under varying conditions. Parameters such as the time between the first H_2 detection and TR (warning interval, Δt_{TR}), peak H_2 concentration ($[H_2]_{peak}$), a rate of H_2 concentration increase ($d[H_2]/dt$), the first H_2 detection time (t_{H2}), time at thermal runaway (t_{TR}) and cell temperature provide deeper insights into gas transport dynamics and safety margins but have not been systematically analyzed.
- H_2 detection is often performed without cross-verification using species-resolved methods such as in situ mass spectrometry (MS), which makes one question whether the sensor signals truly correlate with specific decomposition reactions. This limits the mechanistic confidence needed for sensor integration into battery management systems (BMSs).

In parallel with external gas monitoring, several studies have explored internal or embedded sensing approaches for early fault detection in lithium-ion batteries, including internal temperature probes, strain sensors, pressure monitoring, and impedance-based diagnostics [34]. While such approaches may enable earlier detection of internal degradation processes, their practical implementation often requires cell-level modification and presents challenges related to sensor integration, electrical isolation, and long-term reliability. In contrast, external gas sensing provides a non-invasive and system-compatible strategy for detecting chemically specific off-gas signatures associated with early-stage degradation and pre-thermal-runaway reactions.

This study overcomes these limitations, presenting a multidimensional early-TR-detection framework based on H_2 sensing. This framework is tested at four controlled heating rates (5, 7, 10, 15 °C/min) using $LiNi_{0.8}Mn_{0.1}Co_{0.1}O_2$ (NCM811) cells. A highly selective fast-response Pd–SnO_2 nanorod sensor is used to track H_2 generation in real time, and in situ MS is used to simultaneously monitor H_2, CH_4, CO, and CO_2, providing validation and mechanistic insights [35]. A quantitative correlation is established between heating rate and Δt_{TR}, revealing sensor lead time compression under accelerated-TR conditions. A transition to a gas accumulation regime, where transport limitations cause sharp increases in $[H_2]$ and decreases in Δt_{TR}, is identified at heating rates above 10 °C/min. In situ MS is used for the real-time verification of decomposition pathways, confirming that H_2 is the earliest and most reliable TR indicator. The proposed two-stage diagnostic framework integrates time-resolved hydrogen indicators (t_{H2}, $[H_2]$, and $d[H_2]/dt$) with thermal context, while Δt_{TR} and $[H_2]_{peak}$ are used as post-analysis metrics to evaluate diagnostic robustness across different heating conditions (Fig. 1). By combining real-time sensing with mechanistic validation, this study provides a theoretical understanding of and practical direction for the implementation of H_2-based early-TR-warning systems in next-generation BMSs.

2. Experimental

2.1. H_2 sensor fabrication

H_2 sensor was fabricated by growing Pd-decorated SnO_2 nanorod arrays on Si substrates. A 300 nm–thick insulating SiO_2 layer was thermally grown on Si wafers, and interdigitated Cr/Pt electrodes (30 nm/70 nm) were patterned via photolithography and direct-current magnetron sputtering. SnO_2 nanorods were deposited using SnO_2 granules (99.99%, Kojundo Chemical) as the source via glancing angle deposition (GLAD) at an 80° tilt using an e-beam evaporator (KVE-E2000, Korea Vacuum Tech), with an evaporation rate of 1 Å/s. The as-deposited structures were subsequently crystallized through in-air annealing at 500 °C. A 5 nm–thick Pd (catalytic) layer was subsequently sputtered onto the nanorods and annealed at 200 °C to induce crystallization and enhance dispersion (Fig. S1).

The fabricated sensors exhibited vertically aligned nanorod structures with uniform Pd coverage, as confirmed by instrumental analyses (Fig. S2). Gas sensing performance was evaluated at 80 °C, which corresponds to the optimal operating temperature reported for Pd-decorated SnO_2 nanorod hydrogen sensors, where a favorable balance between sensing response and response/recovery kinetics is achieved [35]. This relatively low operating temperature is attributed to the catalytic dissociation of hydrogen on Pd and the subsequent spillover-assisted reaction on the SnO2 surface [35]. The results revealed reliable H_2 detection in a wide range (1 ppm to 2 vol%) with excellent selectivity over CO, CO_2, and CH_4 (Fig. S3). A calibration curve was constructed to interpret real-time concentration data in TR experiments.

2.2. Pouch cell fabrication and testing

NCM811/graphite single cells with a nominal capacity of ~25 mAh (Fig. 2(a)) were fabricated for heating experiments. A single-sided NCM811 electrode sheet (Custom NANOMYTE® BE-56E, NEI Corporation) consisting of the active material coated on an Al current collector was used as the cathode (areal loading = 11.17 mg/cm^2, capacity = 2.33 mAh/cm^2). A single-sided graphite sheet (Custom BE-200E, NEI Corporation) coated on a Cu current collector was used as the anode (areal loading = 6.84 mg/cm^2, areal capacity = 2.46 mAh/cm^2). Both electrodes were supplied after calendering.

Cell assembly is illustrated in Fig. S4. The electrodes were prepared as shown in Fig. S4(a), and the electrolyte was then injected between the electrodes using a syringe to ensure the complete wetting of the separator and electrode interfaces (Fig. S4(b)). The cathode, separator, and anode were stacked in sequence to construct the full-cell configuration (Fig. S4(c)). The stacked assembly was sealed within a pouch film, and degassing was performed to remove residual gas and complete cell

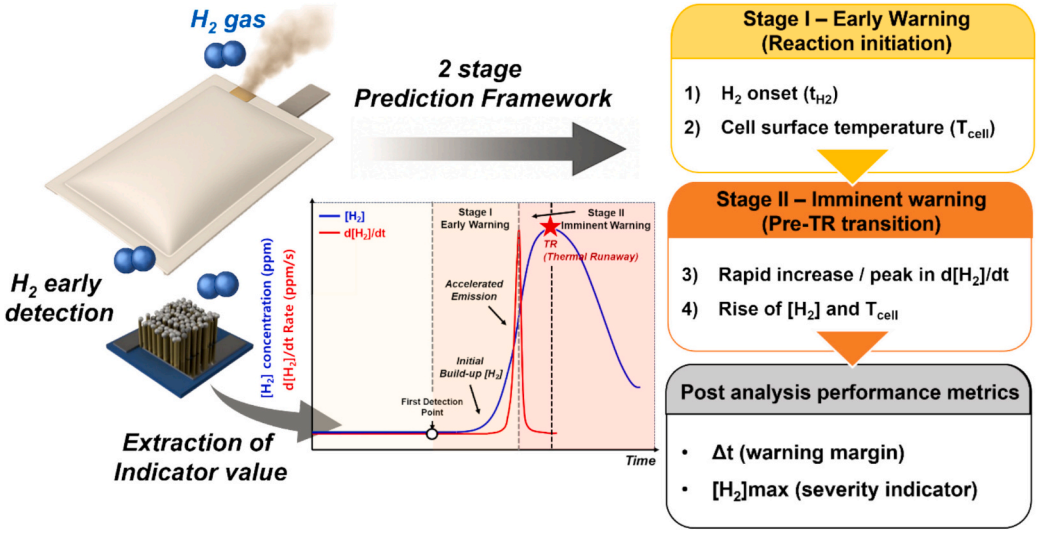

Fig. 1. Schematic representation of a methodology to predict thermal runaway (TR) in lithium-ion batteries via H_2 off-gas detection. By integrating multiple indicators obtained under diverse heating conditions, a two-stage prediction framework is established to capture the progression from early warning to imminent pre-TR states, enabling predictive mitigation of thermal runaway risk.

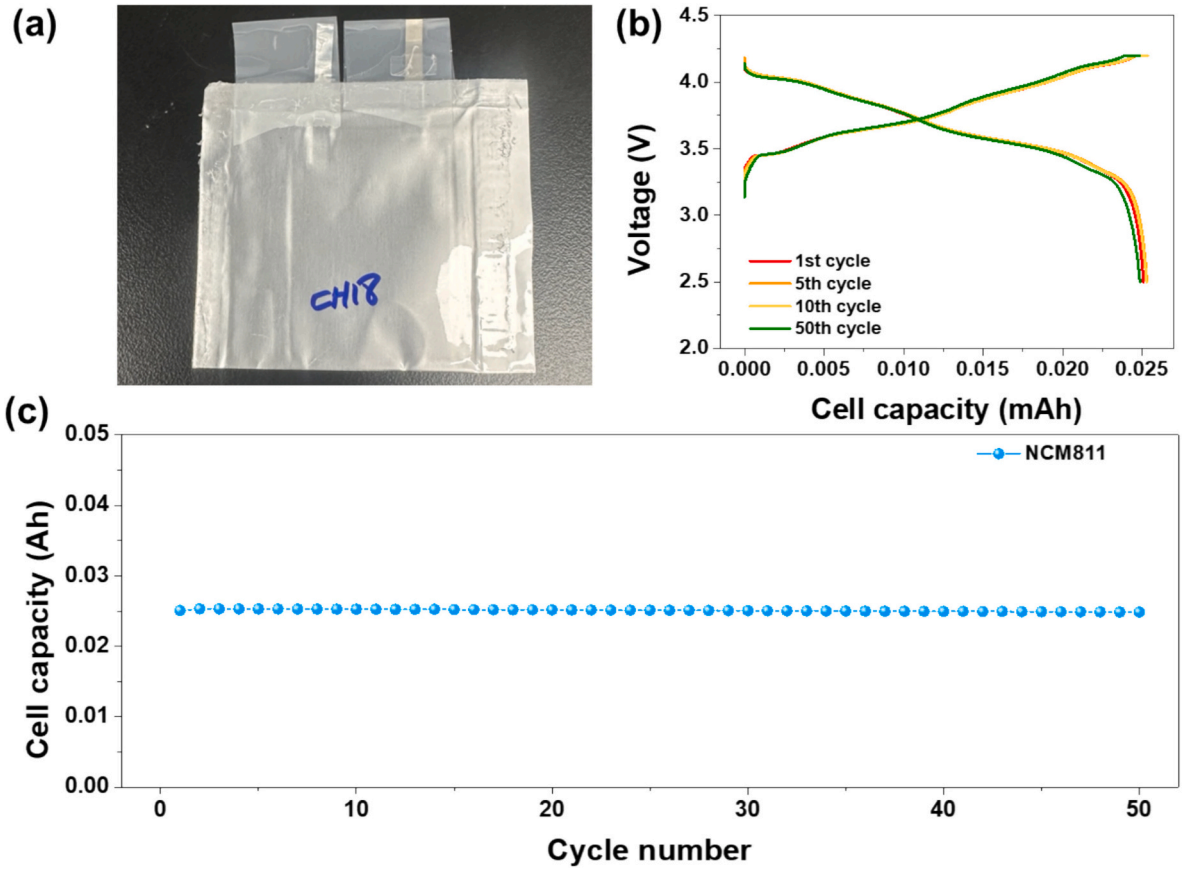

Fig. 2. Electrochemical performance of a representative 25 mAh pouch cell used for TR experiments. (a) As-prepared cell, (b) charge–discharge profiles showing stable initial cycling at 0.2C, and (c) discharge capacity retention over 50 cycles.

fabrication (Fig. S4(d)). After sufficient wetting, a formation process was performed by passing a 0.1C current between 2.5 and 4.2 V under constant current–constant voltage (charge, cut-off current = 0.01C)/ constant current (discharge) conditions. Degassing was subsequently conducted to remove evolved gases and stabilize the internal pressure.

Electrochemical performance was evaluated in a constant-compression state (Fig. 2(b) and (c)). The first-cycle discharge capacity reached ~25 mAh, in good agreement with the nominal capacity, and capacity retention remained above 98% after 50 cycles, which indicated negligible performance degradation. These results demonstrate the reliability of the fabrication process and reproducibility of the NCM811-based single-cell configuration. The assembled cells were then

utilized for controlled heating experiments.

2.3. TR testing

The TR test was designed to simulate controlled thermal abuse of a lithium-ion pouch cell while monitoring gas evolution and temperature responses in real time. A custom-designed TR chamber was used to simulate TR and monitor the associated gas generation in real time. The overall chamber dimensions were 456 × 420 × 320 mm (width × length × height), and the inner chamber measured 190 × 309 × 309 mm. This system (Fig. 3(a)) was purposefully built for LIB safety evaluation and real-time sensing and divided into the lower compartment (Region B, cell test zone) and upper compartment (Region A, gas sensing zone) (Fig. 3(b)). In Region B, an NCM811-based pouch cell was placed on a ceramic heating plate capable of providing controlled heating rates of 5, 7, 10, and 15 °C/min (maximum target temperature = 250 °C). A thermocouple was attached to the cell surface to monitor real-time temperature during TR. The TR onset time (t_{TR}) was defined as the time point at which the cell-surface temperature begins to increase abruptly due to self-heating, indicating the initiation of thermal runaway. Dual outlet lines were used for gas collection and exhaust, ensuring the safe extraction of gases evolved during TR (Fig. 3(d)).

A Pd–SnO_2 H_2 sensor was mounted on the inner wall of the outer chamber (Region A) to spatially isolate it from the heating source and prevent sensor degradation. This configuration minimized thermal interference while maintaining sensing efficiency. A miniature heater integrated into the sensor mount (80 × 50 mm) was used to stabilize sensor operation, while the lower heater module had a footprint of 110 × 80 mm. To stabilize sensor performance, a miniature heating plate was integrated into the sensor mount, and a standard gas inlet was included for calibration purposes. The sensor setup is depicted in Fig. 3 (c). As shown in Fig. 3(c), this inlet line was used only for sensor calibration prior to the thermal runaway (TR) experiments. During calibration (Fig. S3), synthetic air and H_2 were mixed using two mass flow controllers (MFCs) to generate controlled H_2 concentrations (1 ppm–2 vol%).

During TR testing, gases released from the cell in Region B were actively transported through a dedicated transfer tube into Region A. A micro pump system facilitated this upward flow, directing gases through a narrow transfer line toward the sensor and enabling real-time H_2 detection without direct exposure to heat, sparks, or fragments. This spatial separation between gas generation and sensing not only protected the sensor but also reflected a realistic design scenario for BMS integration.

2.4. MS analysis

The gases evolved during controlled heating were identified in real time using an MS-based gas analysis system (Fig. S5). The lower side of the cell was heated using a programmable heater at 10 °C/min. During heating, high-purity Ar was continuously passed at a rate of 5 cc/min, through the single cell to maintain an inert environment and establish a consistent gas flow path from the cell to the MS detector. This purging not only prevented secondary reactions but also enabled the rapid transport of evolved gases to the MS system for real-time analysis. To minimize gas condensation or composition change during transfer and enable the accurate time-resolved monitoring of the gaseous species generated during the thermal process, the gas line connecting the single

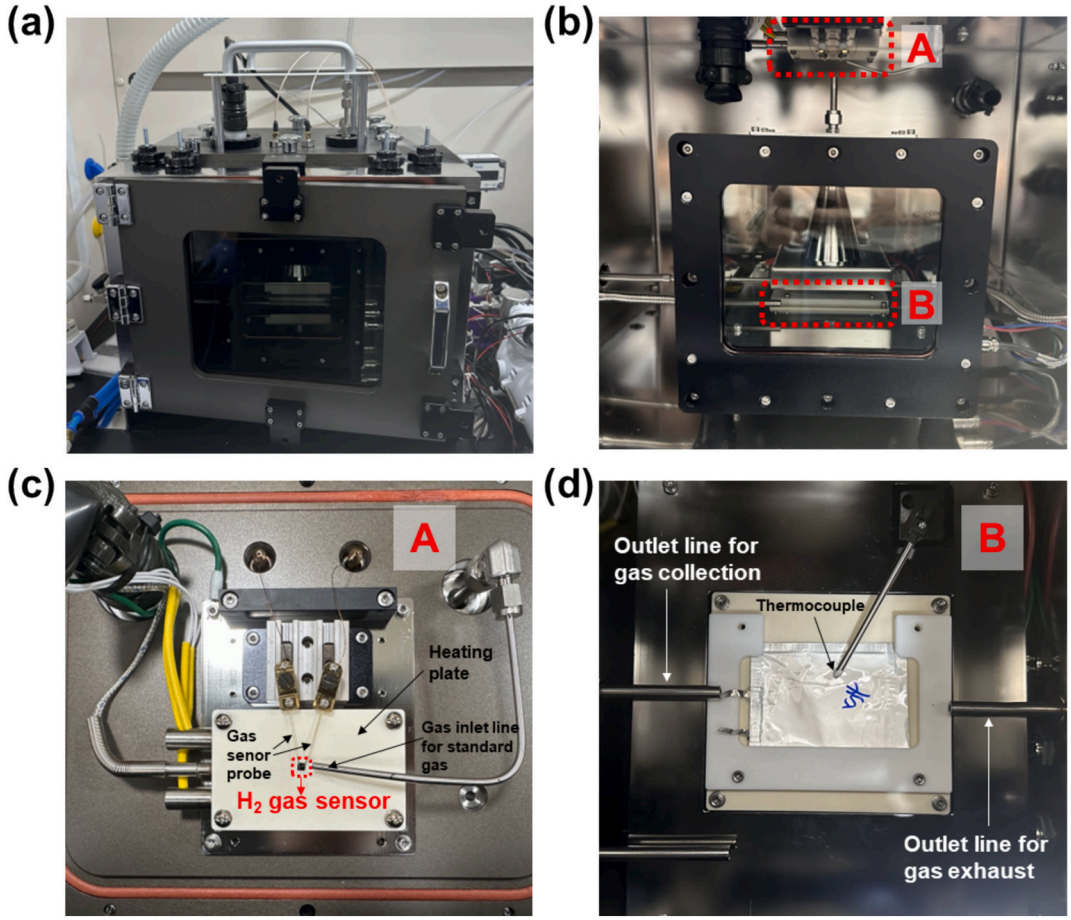

Fig. 3. Custom-designed TR chamber and gas sensing setup. (a) External and (b) internal views of the TR chamber. (c) Gas sensing module mounted on the lid. (d) Heating/overvoltage trigger unit installed inside the chamber.

cell and MS instrument was equipped with a heating block to maintain a uniform temperature throughout the pathway. The detected gases were the products of side reactions occurring during battery heating. By tracing characteristic mass-to-charge (m/z) ratios (m/z = 2 (H_2), 16 (CH_4), 28 (CO), and 44 (CO_2)) within the three-dimensional temperature–time–m/z spectra, we quantitatively analyzed the compositional evolution and release behavior of each gas as a function of temperature. These spectra (Fig. S6) provided insights into the thermal decomposition sequence and corresponding gas evolution pathways within the single cell.

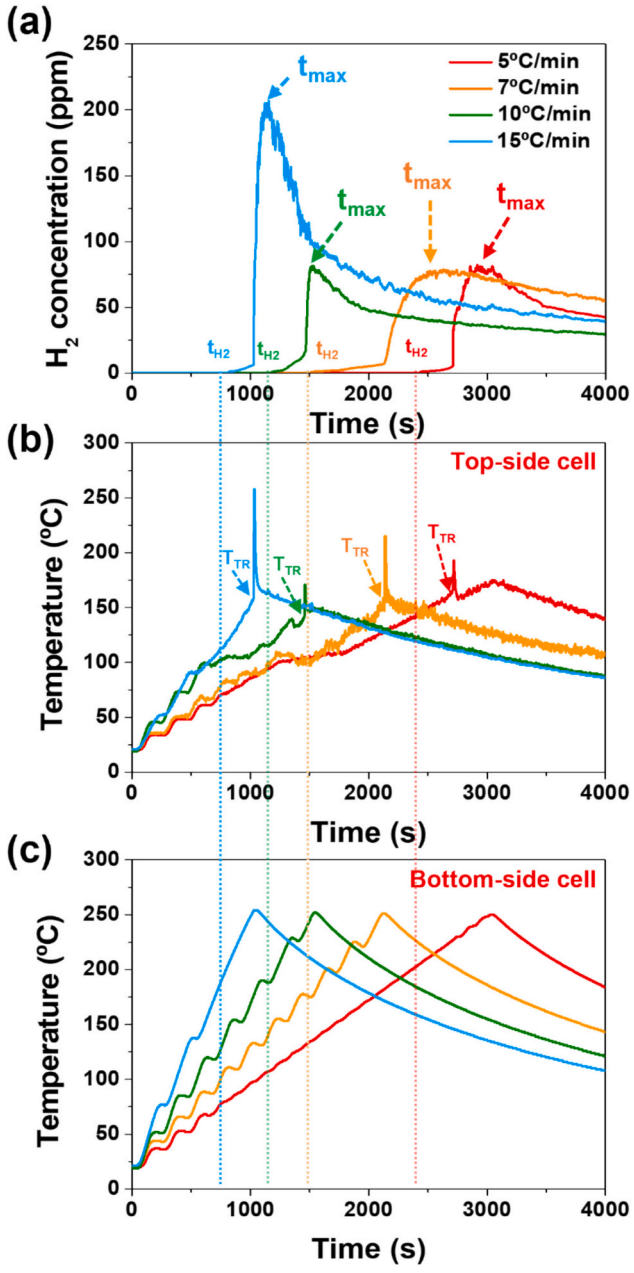

Fig. 4. (a) H_2 concentraion and temperature profiles under TR conditions. (a) H_2 evolution at 5, 7, 10, and 15 °C/min with t_{H2} and t_{max} marked. (b) Top-side and (c) bottom-side cell temperatures under TR.

3. Results and discussion

3.1. H_2 detection and temperature correlation

Fig. 4(a) illustrates the real-time H_2 concentration profiles obtained at heating rates of 5, 7, 10, and 15 °C/min. With the increasing heating rate, H_2 was detected at progressively earlier times (t_{H2}), the first H_2 detection time, and the time required to reach $[H_2]_{peak}$ (t_{max}) notably decreased. This behavior indicates that internal decomposition reactions, particularly those associated with the anode and SEI, were strongly accelerated by heating, consistent with Arrhenius-type kinetics governing exothermic degradation reactions [36]. Upon a heating rate increase from 5 °C/min to 15 °C/min, t_{H2} decreased from 1841 s to 700 s, while the total duration until TR (t_{TR}) decreased from 2711 to 1027, and Δt_{TR} (= t_{TR} – t_{H2}) decreased from 870 s to 327 s. This trend was corroborated by cell surface temperature profiles (Fig. 4(b)), which featured sharp thermal spikes defining the initiation of TR and temporally coinciding with the rapid increase in H_2 concentration [37,38]. Notably, bottom-side temperature (Fig. 4(c)) showed a steeper rise than top-side temperature because of the asymmetric heating configuration (the cell was placed on the heating plate). This setup delayed top-side measurements, reinforcing the necessity of considering thermal diffusion pathways when interpreting surface temperatures as safety indicators and the critical role of H_2 sensing in the early detection of TR [39]. Because the pouch cell is hermetically sealed, gases generated during early-stage decomposition reactions cannot reach the external environment until a venting pathway is formed. Consequently, external detection of H_2 typically occurs close to the venting event, although the gas generation itself begins earlier inside the cell. Nevertheless, the detected H_2 signal still precedes the onset of full thermal runaway and therefore provides a meaningful early warning indicator for abnormal battery behavior.

To quantitatively assess the diagnostic value of the H_2 signal, we extracted and analyzed three key sensing parameters, namely Δt_{TR}, $[H_2]_{peak}$, and $d[H_2]/dt$, as well as a fourth variable, T_{cell}, defined as the concurrently measured cell surface temperature (thermal context). Δt_{TR} reflects the temporal margin available for intervention, $[H_2]_{peak}$ and $d[H_2]/dt$ capture the intensity and dynamics of gas accumulation, respectively, and T_{cell} provides a thermal reference contextualizing whether the TR onset occurs at predictable or anomalously low temperatures. Here, T_{TR} denotes the cell surface temperature at TR onset and is used as a post-analysis reference point when reported. Collectively, these four parameters comprehensively depict the chemical and thermal trajectory of the system under accelerated stress.

With the increasing heating rate in Fig. 4, the four indicators evolved in a nonlinear and coupled manner. Upon a heating rate increase from 10 °C/min to 15 °C/min, Δt_{TR} decreased from 653 s to 327 s, $[H_2]_{peak}$ increased from ~80 ppm to ~207 ppm, and $d[H_2]/dt$ increased ~3.4-fold, indicating a critical acceleration of gas accumulation. Simultaneously, T_{TR} dropped from ~175 °C to 164 °C, implying that TR was triggered earlier relative to absolute cell temperature. The simultaneous time margin contraction, gas signal intensification, and premature thermal failure defines a critical transition regime where the system shifts from a removal-balanced state to an accumulation-dominated state. In this regime, mass transport limitations inhibit outward gas diffusion, leading to a steeper internal pressure buildup and more abrupt thermal feedback.

To formalize this regime, we propose a time-resolved diagnostic interpretation framework in which H_2 onset, $d[H_2]/dt$, and the measured cell temperature (T_{cell}) are interpreted not as independent descriptors but as coupled indicators describing the transition from reaction initiation to accelerated pre-TR behavior. For example, an increase in $[H_2]_{peak}$ without a corresponding steep increase in $d[H_2]/dt$ may represent relatively benign off-gassing, whereas a rapid rise in $d[H_2]/dt$ together with concurrent increases in $[H_2]$ and temperature suggests an accelerated transition toward an imminent pre-TR stage.

In this work, Δt_{TR} (warning margin to TR) and $[H_2]_{peak}$ are primarily treated as post-analysis performance metrics used to evaluate the robustness and consistency of the proposed interpretation across heating conditions, rather than as universally transferable real-time cutoffs. This framework provides a structured basis for defining calibratable early-warning logic under thermal context, while avoiding reliance on a single static gas or temperature limit. The next section expands on this analysis by reformulating these indicators into a two-stage, time-resolved warning framework and identifying operational windows where H_2-based sensing remains reliable for preemptive intervention across heating rates.

3.2. Early-warning thresholds and predictive insights

The four key sensing indicators introduced in Section 3.1 (Δt_{TR}, $[H_2]_{peak}$, $d[H_2]/dt$, and T_{cell}) can be evaluated beyond individual measurements to form a predictive framework for early TR warning. These indicators not only varied with the heating rate but also exhibited coupled nonlinear transitions, especially at 10–15 °C/min. Upon a heating rate increase from 5 °C/min to 15 °C/min, Δt_{max} (t_{max}-t_{H2}) sharply decreased from ~1436 s to 327 s, while $[H_2]_{peak}$ increased from ~80 ppm to ~250 ppm and $d[H_2]/dt$ increased ~3.4-fold, signaling a notable shift in the gas evolution regime (Fig. 5 and Table 1). These changes suggest that the system transitioned from a dissipation-balanced state, where gas generation and removal are matched, to an accumulation-dominated state, where H_2 rapidly builds up because of insufficient venting and thermal management [40–42].

This regime shift originates from the temporal overlaps of multiple low-temperature exothermic reactions. In particular, SEI decomposition reactions, including Li_2CO_3 (229.4 J/g), LMC (143.4 J/g), and LEMC (46.2 J/g) decomposition, begin at 40 °C–120 °C and release measurable amounts of H_2 and CO_2 [43]. At higher temperatures, additional reactions such as binder decomposition (>300 °C, ~40 J/g), EC/EMC-based electrolyte breakdown (150 °C–310 °C), and NCM811 cathode transformations (250 °C–350 °C, >2000 J/g) release O_2 and amplify thermal feedback [44]. Importantly, H_2 evolution is not limited to a narrow reaction window but rather spans multiple overlapping mechanisms on anode and cathode sides.

These temporally overlapping reactions (from early SEI decomposition to O_2 release from the cathode) constitute a thermochemical cascade. Their dynamic alignment with sensor data supports that the Δt_{TR} and Δt_{max} decrease, $[H_2]_{peak}$ surge, and $d[H_2]/dt$ increase are not just empirical signals but rather mechanistic reflections of the transition from balanced degradation to an accumulation dominated pre-TR runaway. Table 2 and Fig. 8 illustrate this correspondence across gas species, thermal phases, and sensor responses.

Table 1
Time interval between H_2 detection (t_{H2}) and TR onset (t_{TR}) and peak H_2 concentrations at different heating rates.

Heating rate (°C/min)	Time interval between t_{H2} and t_{TR} (Δt_{TR}) (s)	H_2 concentration at t_{max} (ppm)
5	~1436	~81
7	~1201	~98
10	~685	~87
15	~327	~250

Table 2
Literature-reported gas generation reactions associated with the temperature range probed by MS in this study.

m/z	Reaction equation	Temperature (°C)	Mechanism	Reference
2 (H_2)	Li + (–CF_2CH_2–) → 0.5$H_{2\ (g)}$ + LiF + (–CH=CF–)	≥35 °C	Li dendrite–binder reaction triggers early H_2 release	[27]
	Li + (–CF_2CH_2–)$_2$ → $H_{2\ (g)}$ + LiF + (–CH=CH–CH=CH–)	≥170 °C	Li dendrite–binder reaction triggers early H_2 release	[38]
	CMC–OH $_{(s)}$ + Li → CMC–OLi $_{(s)}$ + 0.5$H_{2\ (g)}$	≥260 °C	Li dendrite–binder reaction triggers early H_2 release	[44]
	(–CH_2CH_2O–)$_n$ → $H_{2\ (g)}$ + CH_x + CO $_{(g)}$ + H_2O + (–CH_2O–)$_{n-2}$	40 °C–170 °C	SEI decomposition induces early H_2 release	[38]
	2ROH + Li → $H_{2\ (g)}$ + 2ROLi	≥142 °C	SEI decomposition induces early H_2 release	[44]

As the heating rate increases, these reactions begin to merge temporally rather than unfold sequentially. Upon a heating rate increase from 5 °C/min and 10 °C/min, Δt_{TR} notably decreased (by ~1000 s), but $[H_2]_{peak}$ remained stable, which suggests that the system still effectively dissipated heat and gases. However, at 15 °C/min, the sharp increase in $[H_2]_{peak}$ (~207 ppm) indicated that internal gas transport limitations (e.g., separator shrinkage at 135 °C–200 °C, electrolyte viscosity rise, narrowing venting paths) began to dominate [45]. These constraints reduced H_2 removal efficiency and increased the local accumulation of gas near the sensor.

This shift is tightly coupled with the feedback dynamics of thermal degradation. Upon heating, the Arrhenius behavior of reaction rates

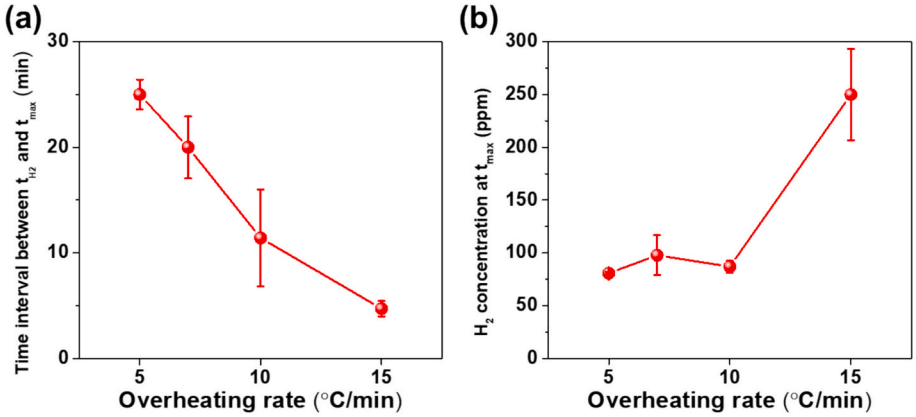

Fig. 5. (a) Time interval from initial H_2 detection (t_{H2}) to the time of maximum H_2 concentration (t_{max}), and (b) peak H_2 concentration as functions of heating rate. Data points represent mean values obtained from repeated tests (n) for each condition (see Table S1), and error bars represent the standard deviation (SD) of repeated measurements.

causes the acceleration of gas and heat generation. At this point, the sensor data reflect not only how much H_2 is being produced but also how poorly it is being evacuated. Thus, the Δt_{TR} reduction, $[H_2]_{peak}$ surge, and $d[H_2]/dt$ increase collectively indicate a critical state transition. From a diagnostic perspective, this suggests that no single metric is sufficient for early TR detection. Instead, the joint interpretation of Δt_{TR}, $[H_2]_{peak}$, $d[H_2]/dt$, and temperature rise rate provides a more robust predictive basis.

To strengthen the scientific basis of early-warning threshold design, the indicators are interpreted within a two-stage, time-resolved warning framework that explicitly couples hydrogen evolution behavior with thermal context. The proposed logic is presented as a calibratable methodology rather than a universal, condition-invariant threshold.

The values extracted from the present dataset (e.g., heating-rate-dependent Δt_{TR}, $[H_2]_{peak}$, and $d[H_2]/dt$ peak behavior) are therefore treated as condition-specific operational examples and post-analysis evaluation references, rather than universally transferable thresholds. Given the inherent variability of abuse-type TR experiments—even under nominally identical protocols—temperature is treated as a contextual variable rather than a fixed-temperature cutoff for universal prediction.

Within this staged logic, Stage I (early warning) emphasizes H_2 onset and sustained post-onset growth under the prevailing thermal context, whereas Stage II (imminent warning) focuses on the rapid rise and peak in $d[H_2]/dt$ together with concurrent increases in $[H_2]$ and temperature.

To further support the scientific grounding of this interpretation, preliminary thermal runaway (TR) prediction modeling was conducted based on the reaction-kinetic framework reported in Ref. [44], which describes gas evolution during thermal decomposition of battery components using Arrhenius-type reaction kinetics (see Table S2). Model-inferred internal hydrogen evolution features (e.g., onset and peak generation timing) were compared with the timing of externally measured exhaust H_2 signals (Fig. 6).

The modeling comparison provides supporting evidence for the time-resolved hydrogen generation kinetics—particularly the evolution of $d[H_2]/dt$—underlying the proposed two-stage warning logic. A measurable time offset was observed, which is reasonably attributed to the intrinsic delay associated with internal gas accumulation, vent/release pathway formation, and subsequent transport and mixing prior to external detection.

This interpretation is corroborated by in situ MS data (Section 3.3). H_2 was detected as early as ~70 °C, well before other gases, and its peak rapidly intensified near 140 °C. This behavior aligns with the thermochemical sequence of SEI breakdown followed by electrolyte decomposition and cathode collapse, highlighting H_2 as the earliest and most dynamically responsive indicator [27,38].

In summary, as TR evolves, the internal reaction landscape becomes increasingly coupled and compressed in time. H_2 evolution, owing to its low-temperature onset and correlation with SEI/anode reactions, offers a unique early signal. By providing Δt_{TR}, $[H_2]_{peak}$, $d[H_2]/dt$, and T_{cell}, H_2

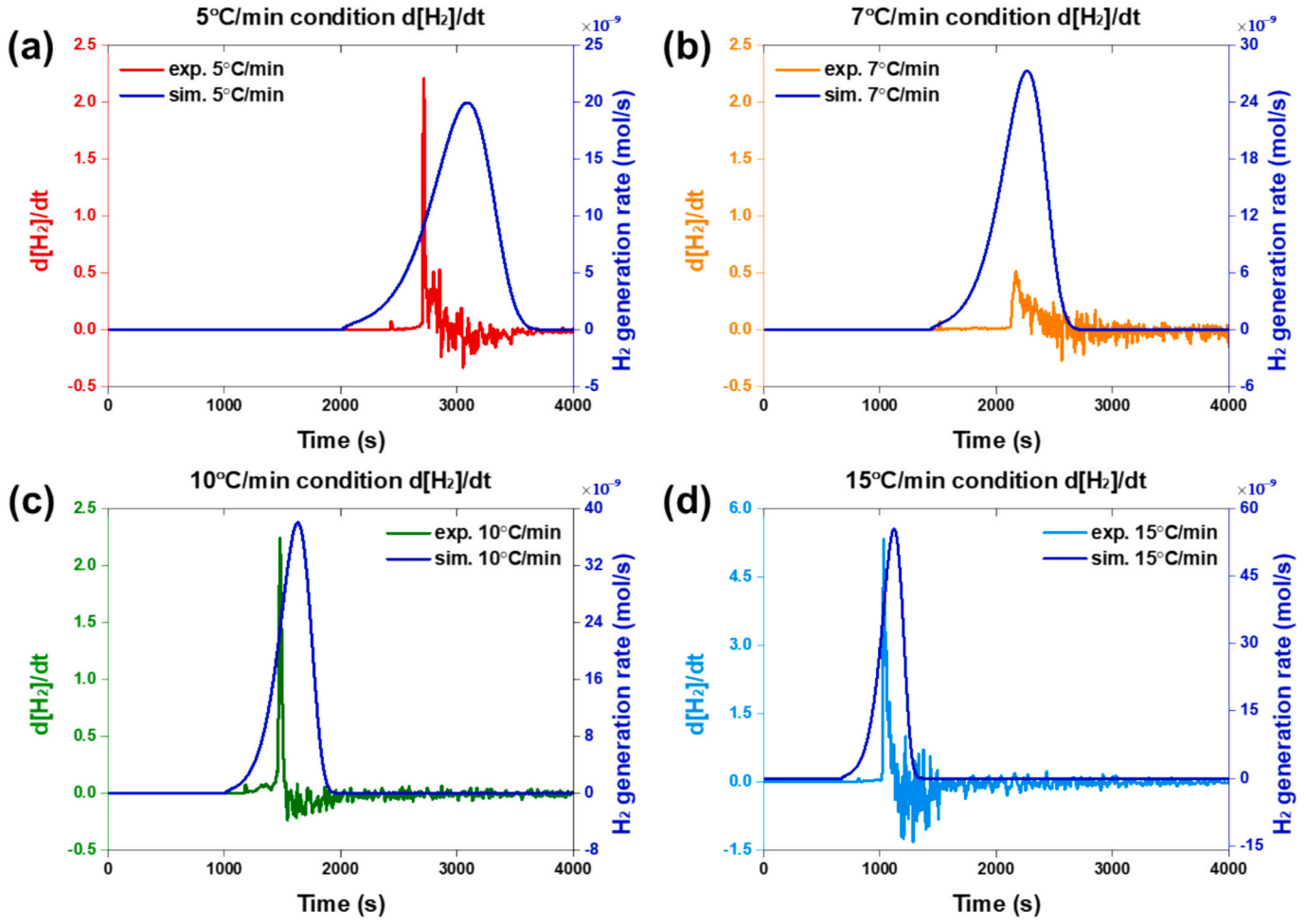

Fig. 6. Experimental–model comparison of hydrogen evolution kinetics under different heating rates. The experimentally derived $d[H_2]/dt$ from the sensor-measured exhaust H_2 concentration is shown as the colored solid line (left axis, ppm s^{-1}), while the model-predicted H_2 generation rate calculated from the internal temperature history is shown as the blue solid line (right axis, mol s^{-1}; $\times 10^{-9}$ scaling) during temperature ramping at heating rates of (a) 5 °C/min, (b) 7 °C/min, (c) 10 °C/min, and (d) 15 °C/min. (For interpretation of the references to colour in this figure legend, the reader is referred to the web version of this article.)

sensing enables the establishment of a multiparametric early-warning platform capable of not only detecting but also predicting TR onset under variable real-world conditions. This predictive capacity supports the practical implementation of H_2-based safety mechanisms in next-generation LIBs. Together, these indicators—Δt_{TR}, $[H_2]_{peak}$, and d $[H_2]$/dt—can be synthesized into a unified diagnostic metric such as the Thermal Gas Accumulation Index (TGAI), serving as a quantitative precursor to critical thermal transitions.

3.3. In situ MS analysis

Building on the diagnostic indicators defined in Section 3.2 (Δt_{TR}, $[H_2]_{peak}$, $d[H_2]/dt$, and T_{cell}), the present section validates the physical credibility of H_2-based early TR detection through in situ MS analysis. The sensor data reveal trends in H_2 concentration and warning interval, while MS analysis provides the species-resolved confirmation of gas evolution pathways, verifying the timing and mechanism of H_2 release during pre-TR phases.

H_2 ($m/z = 2$) was first detected by MS at ~70 °C, well below the typical TR threshold of >180 °C (Fig. 7), indicating that H_2 can serve as an early pre-TR indicator. Based on prior reports, H_2 evolution in the low-temperature region has been associated with early interfacial decomposition processes (e.g., SEI breakdown). Additional lithium-related side reactions reported in the literature may also contribute to early H_2 generation under certain electrochemical conditions [11,40]. By comparison, the external Pd–SnO_2 sensor exhibited an apparent H_2 onset near ~100 °C (Section 3.1), corresponding to the measurable release of gas under externally imposed heating. This offset arises from differences in sampling configuration and gas transport dynamics rather than from fundamentally different H_2-generation mechanisms. Early-stage interfacial reactions may generate trace H_2 within the sealed pouch cell at lower temperatures; however, the external sensor registers H_2 only after sufficient outward release and local accumulation occur near the sensing location. Therefore, the sensor-based onset represents the practically relevant signal for external early-warning configurations, whereas the MS onset reflects the earliest detectable internal gas generation. A sharp H_2 signal intensification was observed around 141 °C, coinciding with accelerated SEI and electrolyte decomposition, which further reinforces the role of H_2 as an early-stage chemical precursor [44,46].

Comprehensive species-resolved analysis (Fig. S6) revealed that multiple gases, including H_2 ($m/z = 2$), CH_4 ($m/z = 16$), CO/C_2H_4 ($m/z = 28$), and CO_2 ($m/z = 44$), were generated almost simultaneously across the 100 °C–200 °C range. CH_4 emerged at intermediate temperatures (100 °C–150 °C), while overlapping $m/z = 28$ peaks indicated the concurrent presence of CO and C_2H_4 and were attributed to electrolyte decomposition pathways involving EC and DMC. CO_2 showed the most intense and sustained signal, with initial release aligned with SEI degradation (90 °C–130 °C) and continued evolution from electrolyte and separator breakdown at higher temperatures [47–49].

Despite this multiplex gas evolution, the Pd–SnO_2 sensor consistently registered H_2 ahead of other volatiles. This behavior is not merely an artifact of sensor sensitivity but has two fundamental reasons. First, the low molecular weight and large diffusion coefficient (~0.61 cm^2/s at 25 °C in air) of H_2 allow it to travel through cell layers more quickly than larger molecules such as hydrocarbons or CO_2 and reach the sensor earlier. Second, the Pd-functionalized SnO_2 nanostructure was engineered to preferentially react with H_2 via spillover mechanisms and catalytic dissociation, providing a rapid response and selective detection in mixed-gas environments [35].

This dual advantage explains why H_2 was consistently the earliest and most reliably detected species in sensor outputs even under the complex conditions of overlapping gas evolution. As shown in Section 3.2, when the heating rate increased from 10 °C/min to 15 °C/min and Δt_{TR} dropped to <400 s, the detection window became extremely narrow. In such scenarios, the identity of the gas detected first is critical for initiating timely mitigation. The physical properties of H_2 and engineered sensor response ensure that early warning is not only possible but also predictive. Moreover, the low ignition energy (~0.02 mJ) and broad flammability range (4–75 vol% in air) of H_2 make it the most dangerous among early evolving gases, further justifying its prioritization in safety systems.

In conclusion, MS analysis confirmed that H_2 is not only the first species to evolve during TR precursors but also the one most detectable in practice because of its physicochemical properties and sensor affinity. These findings substantiate the use of H_2 sensing as a scientifically grounded and technically reliable strategy for early TR warning, supporting its integration into advanced BMS architectures.

3.4. Comparative analysis with alternative TR monitoring strategies

Building on the time-resolved hydrogen sensing results (Sections

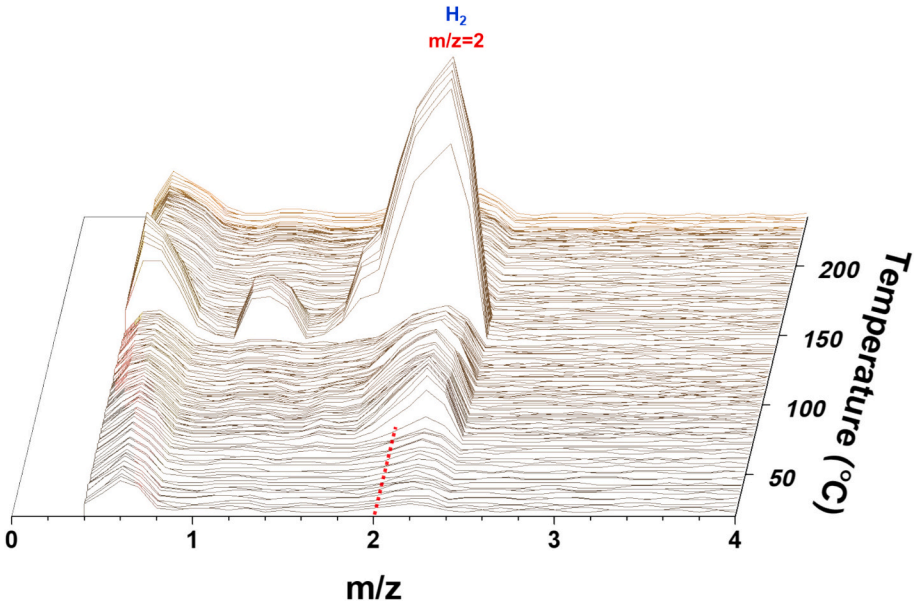

Fig. 7. In situ mass spectra of gases evolved during pouch cell overheating (10 °C/min, max 230 °C) in the m/z range of 0–4.

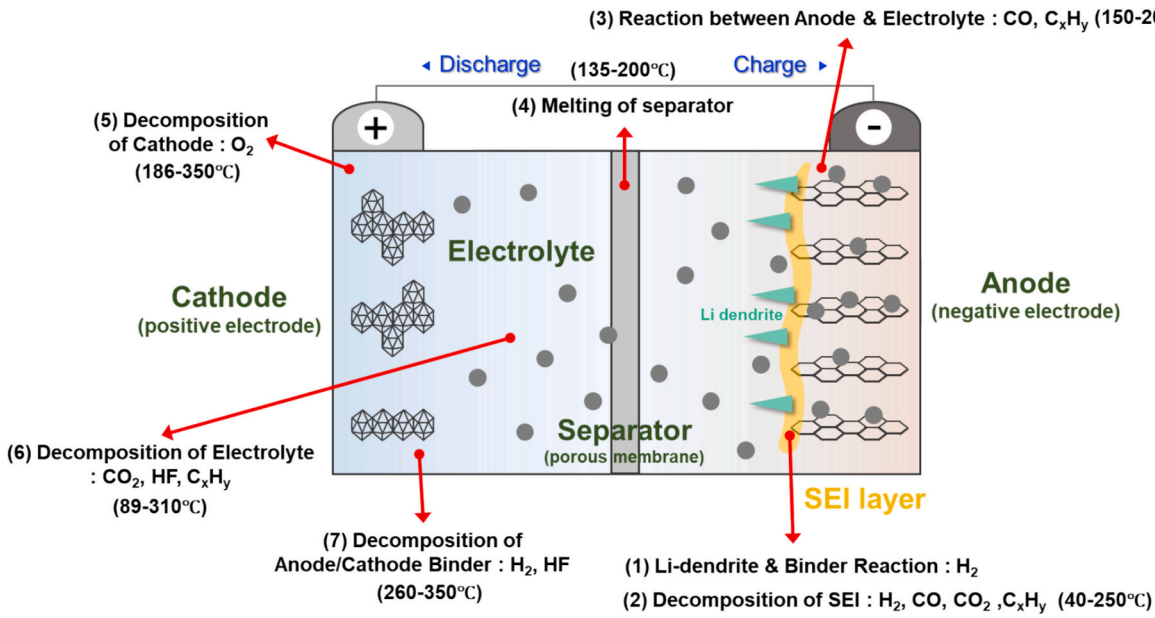

Fig. 8. Schematic of the TR and corresponding gas generation mechanisms.

3.1–3.2) and their consistency with in situ MS observations (Section 3.3), we position the proposed Pd–SnO_2 H_2 sensing approach relative to representative TR monitoring strategies. Because different modalities interrogate distinct physical variables along the TR cascade, a meaningful comparison should emphasize earliness, mechanistic interpretability, robustness to boundary-condition variability, and practical integrability under abuse conditions rather than assuming that any single signal is universally sufficient [50].

Conventional TR monitoring strategies can be broadly categorized into thermal, electrical, and mechanical/pressure-based approaches. Temperature monitoring (e.g., thermocouples, RTDs, IR methods) remains indispensable for contextualizing degradation severity and boundary conditions [51,52], but is inherently limited by thermal inertia and heat-transfer delay. Electrical diagnostics, including voltage anomalies and impedance-related indicators, are attractive because of their direct compatibility with BMS architectures and ability to capture circuit-level abnormalities [53,54]. Mechanical or pressure-related signals (e.g., swelling, pressure rise, or vent signatures) provide clear evidence of internal gas accumulation and release processes and serve as strong imminent-risk indicators [55,56]. However, these modalities differ in their earliest diagnostic sensitivity: thermal and mechanical channels often become prominent near acceleration or venting stages, whereas electrical signals may not always uniquely correspond to the earliest interfacial decomposition pathways across chemistries.

In this context, hydrogen sensing provides a complementary chemical–kinetic axis for early-stage diagnosis. As demonstrated in Sections 3.1–3.3, H_2 is detected as one of the earliest evolving species and intensifies prior to full TR onset. Its time-resolved kinetics, including d[H_2]/dt behavior, offer actionable information beyond a single concentration threshold. Importantly, the present contribution is not framed as replacing established monitoring channels, but as integrating hydrogen evolution features with thermal context through a structured two-stage warning framework (Section 3.2). Consistency with in situ MS observations further supports the mechanistic interpretability of this staged logic.

From a practical implementation perspective, the present metal-oxide semiconductor (MOS)-based sensing platform offers additional advantages in manufacturability and system integration. Unlike laboratory-scale mass spectrometry systems or optical fiber-based early-warning devices, the Pd–SnO_2 nanorod sensor can be fabricated using batch-compatible thin-film processes, including thermal oxidation, photolithography, sputtering, and GLAD deposition. The device structure—comprising a thermally grown SiO_2 layer, Cr/Pt interdigitated electrodes, vertically aligned SnO_2 nanorods, and a thin Pd catalytic layer—is fully compatible with conventional semiconductor processing. Importantly, the fabrication does not require vacuum-sealed optical cavities, complex optical alignment procedures, or highly specialized transistor architectures.

Although certain FET-based or optical sensing platforms may achieve lower detection limits, the proposed Pd–SnO_2 architecture provides a balanced trade-off among sensitivity (ppm-level), response speed, selectivity, scalability, and system cost. Such balance is particularly important for module- or pack-level integration in practical battery systems, where manufacturability, reliability, and cost efficiency are as critical as detection sensitivity.

From a practical standpoint, the proposed sensor platform is most appropriately deployed as a complementary early-warning channel alongside temperature and electrical monitoring. Temperature provides essential boundary-condition context, electrical signals capture circuit-level anomalies relevant to protection logic, and hydrogen kinetics can extend warning margin and sharpen imminent-risk discrimination when interpreted within the staged framework. Future work should expand validation across broader cell formats and chemistries and establish calibration procedures that map staged decision variables to application-specific constraints such as installation geometry and acceptable false-alarm tolerance [50,57,58]. In parallel, integrating hydrogen-based indicators with thermal, electrical, or pressure signals in a sensor-fusion framework is expected to enhance robustness at module- and pack-level deployment.

Finally, recent studies have shown that embedded (internally inserted) temperature sensing can provide earlier and more representative thermal information than external surface measurements under certain abuse scenarios [59,60]. Analogously, while the present study focuses on external exhaust monitoring, the development of embedded or in-cell gas sensing concepts (e.g., for H_2 evolution) may enable even earlier detection of interfacial reaction precursors. If implemented safely without compromising cell integrity, such approaches could further advance hydrogen-based TR prediction beyond external indicators [61].

4. Conclusions

This study demonstrates that TR in LIBs is preceded by H_2 evolution,

revealing the utility of this phenomenon as a quantifiable and reliable early-warning signal across diverse heating conditions. A Pd-decorated SnO_2 nanorod sensor with ppm-level sensitivity is used to monitor real-time H_2 evolution in NCM811 cells at controlled heating rates of 5, 7, 10, and 15 °C/min. Across these conditions, the H_2-based warning interval Δt_{TR} ($t_{TR} - t_{H2}$) remains consistently nonzero, decreasing from 1436 s (~24 min) to 327 s (~5.5 min) as the heating rate increases from 5 °C/min to 15 °C/min, thus offering a viable temporal window for preemptive intervention even under rapid escalation scenarios.

A critical transition in gas evolution behavior is observed with the increasing heating rate. Below 10 °C/min, $[H_2]_{peak}$ remains stable (~80 ppm), reflecting a removal-balanced regime. However, at 15 °C/min, $[H_2]_{peak}$ surges to ~207 ppm, indicating a shift to an accumulation-dominated state due to thermal feedback, venting limitations, and overlapping reaction kinetics. This trend is paralleled by a steep rise in $d[H_2]/dt$. Collectively, the changes in the above metrics mark an approach to the TR threshold.

In situ MS analysis validates these findings, identifying H_2 as the earliest-evolving gas initially detected at ~70 °C, i.e., far below typical TR onset temperatures. Despite the simultaneous emergence of CH_4, CO, and CO_2 at higher temperatures, H_2 is consistently detected first because of its low molecular weight and superior diffusivity, as well as the high selectivity of the Pd–SnO_2 sensor. These characteristics position H_2 not only as a leading indicator of early degradation but also as the most dynamically responsive species under TR-relevant conditions.

To move beyond binary detection schemes, we propose a multiparameter sensing framework integrating Δt_{TR}, $[H_2]_{peak}$, and $d[H_2]/dt$ into a unified risk assessment strategy. This approach enables robust decision-making by capturing the timing and intensity of TR precursors, particularly in critical transition zones where intervention time sharply narrows. A simplified generation–removal model supports this interpretation and provides a physical basis for sensor threshold design.

In summary, H_2 sensing coupled with a multidimensional analysis of timing and concentration dynamics offers a promising path toward predictive safety systems for LIBs. Future work should focus on scaling the proposed sensing framework to module-level validation using high-capacity cells and evaluate its predictive performance under integrated thermal and electrical conditions. Future studies will focus on validating this approach at the battery module level with increased cell capacity and realistic enclosure designs, ensuring seamless integration into practical BMS platforms.

CRediT authorship contribution statement

Sanghyun Park: Writing – original draft, Visualization, Investigation, Data curation. **Mingi Kim:** Investigation, Data curation, Writing – review & editing. **Je-seong Oh:** Writing – original draft, Visualization, Investigation, Data curation. **Minuk Kim:** Writing – review & editing, Validation, Conceptualization. **Kyung-Ho Park:** Visualization, Data curation. **Kwang-young Yoo:** Visualization, Data curation. **Min-Jae Kim:** Investigation, Data curation. **Keunhyung Lee:** Investigation, Data curation. **Mi-Sung Kim:** Investigation, Data curation. **Hyun-Sook Lee:** Visualization, Conceptualization, Supervision, Validation, Writing – review & editing. **Jongsup Hong:** Writing – review & editing, Validation, Supervision, Conceptualization. **Wooyoung Lee:** Writing – review & editing, Validation, Supervision, Conceptualization.

Declaration of Generative AI and AI-assisted technologies in the writing process

The authors used ChatGPT (OpenAI) to assist in language editing during the preparation of this manuscript. The authors reviewed and verified the content generated by the AI to ensure its accuracy and appropriateness for scientific communication.

Declaration of competing interest

The authors declare that they have no known competing financial interests or personal relationships that could have appeared to influence the work reported in this paper.

Acknowledgments

This work was supported by the National Research Foundation of Korea (NRF), funded by the Korean government (Ministry of Science and ICT, MSIT) (No. NRF-2022M3H4A3053304, National Core Materials Research Center, Platform Type). Additional support was provided by the Commercialization Promotion Agency for R&D Outcomes (COMPA), funded by MSIT (No. RS-2025-02633929); the Research and Development Program under the National Fire Agency (No. RS-2024-00404040), funded by the Ministry of the Interior and Safety (MOIS, Korea). This work was also supported by Korea Basic Science Institute (National research Facilities and Equipment Center) grant funded by the Ministry of Science and ICT (No. RS-2024-00403098). H.-S. Lee acknowledges support from the NRF, funded by MSIT (No. RS-2025-00555865).

Appendix A. Supplementary data

Supplementary data to this article can be found online at https://doi.org/10.1016/j.est.2026.122082.

Data availability

Data will be made available on request.

References

[1] A. Manthiram, An outlook on lithium ion battery technology, ACS Cent. Sci. 3 (2017) 1063–1069, https://doi.org/10.1021/acscentsci.7b00288.
[2] M. Hasan, M. Mahmud, A. Mahmud, S. Habib, S. Islam Motakabber, Review of electric vehicle energy storage and management system: standards, issues, and challenges, J. Energy Storage 41 (2021) 102940, https://doi.org/10.1016/j.est.2021.102940.
[3] Y. Tian, G. Zeng, A. Rutt, T. Shi, H. Kim, J. Wang, J. Koettgen, Y. Sun, B. Ouyang, T. Chen, Z. Lun, Z. Rong, K. Persson, G. Ceder, Promises and challenges of next-generations "beyond Li-ion" batteries for electric vehicles and grid decarbonization, Chem. Rev. (2020), https://doi.org/10.1021/acs.chemrev.0c00767.
[4] J. Xu, X. Cai, S. Cai, Y. Shao, C. Hu, S. Lu, S. Ding, High-energy Lithium-ion batteries: recent progress and a promising future in applications, Energy Environ. Mater. 6 (2023), https://doi.org/10.1002/eem2.12450.
[5] J. Wen, D. Zhao, C. Zhang, An overview of electricity powered vehicles: lithium-ion battery energy storage density and energy conversion efficiency, Renew. Energy 162 (2020) 1629–1648, https://doi.org/10.1016/j.renene.2020.09.055.
[6] Y. Ding, Z. Cano, A. Yu, J. Lu, Z. Chen, Automotive Li-ion batteries: current status and future perspectives, Electrochem. Energy Rev. 2 (2019) 1–28, https://doi.org/10.1007/s41918-018-0022-z.
[7] C. Liu, J. Sun, P. Zheng, L. Jiang, H. Liu, J. Chai, Q. Liu, Z. Liu, Y. Zheng, X. Rui, Recent advances of non-lithium metal anode materials for solid-state lithium-ion batteries, J. Mater. Chem. A (2022), https://doi.org/10.1039/d2ta03905b.
[8] P. Lyu, X. Liu, J. Qu, J. Zhao, Y. Huo, Z. Qu, Z. Rao, Recent advances of thermal safety of lithium ion battery for energy storage, Energy Storage Mater. 31 (2020) 195–220, https://doi.org/10.1016/j.ensm.2020.06.042.
[9] S. Shahid, M. Agelin-Chaab, A review of thermal runaway prevention and mitigation strategies for lithium-ion batteries, Energy Convers. Manage.: X (2022), https://doi.org/10.1016/j.ecmx.2022.100310.
[10] X. Feng, D. Ren, X. He, M. Ouyang, Mitigating thermal runaway of lithium-ion batteries, Joule 4 (2020) 743–770, https://doi.org/10.1016/j.joule.2020.02.010.
[11] Z. Zhang, W. Zhao, Y. Ma, Y. Yao, T. Yu, W. Zhang, H. Guo, X. Duan, R. Yan, D. Xu, M. Chen, A flexible integrated temperature-pressure sensor for wearable detection of thermal runaway in lithium batteries, Appl. Energy 381 (2025) 125191, https://doi.org/10.1016/j.apenergy.2024.125191.
[12] Z. Cheng, L. Ju, J. Li, P. Qin, Z. Zhao, W. Mei, H. Bao, K. Jin, X. Meng, Q. Wang, Early warning of thermal runaway for larger-format lithium iron-phosphate battery by coupling internal pressure and temperature, Appl. Energy 383 (2025) 125396, https://doi.org/10.1016/j.apenergy.2025.125396.
[13] Y. Li, L. Jiang, N. Zhang, Z. Wei, W. Mei, Q. Duan, J. Sun, Q. Wang, Early warning method for thermal runaway of lithium-ion batteries under thermal abuse condition based on online electrochemical impedance monitoring, J. Energy Chem. 92 (2024) 74–86, https://doi.org/10.1016/j.jechem.2023.12.049.

[14] N. Kisseler, F. Hoheisel, C. Offermanns, M. Frieges, H. Heimes, A. Kampker, Monitoring of thermal runaway in commercial prismatic high-energy lithium-ion battery cells via internal temperature sensing, Batteries (2024), https://doi.org/10.3390/batteries10020041.

[15] T. Jia, Y. Zhang, Chuyuan, H. Yu, S. Hu, The early warning for thermal runaway of lithium-ion batteries based on internal and external temperature model, J. Energy Storage (2024), https://doi.org/10.1016/j.est.2024.110690.

[16] W. Mei, Z. Liu, C. Wang, C. Wu, Y. Liu, P. Liu, X. Xia, X. Xue, X. Han, J. Sun, G. Xiao, H. Tam, J. Albert, Q. Wang, T. Guo, Operando monitoring of thermal runaway in commercial lithium-ion cells via advanced lab-on-fiber technologies, Nat. Commun. 14 (2023), https://doi.org/10.1038/s41467-023-40995-3.

[17] S. Wang, Z. Shi, M. Chen, X. Han, L. Zhao, J. Wang, Research on a MEMS pressure sensor for fast thermal runaway detection for lithium-ion batteries, J. Phys. Conf. Ser. 2954 (2025), https://doi.org/10.1088/1742-6596/2954/1/012043.

[18] B. Gulsoy, H. Chen, C. Briggs, T. Vincent, J.E.H. Sansom, J. Marco, Real-time simultaneous monitoring of internal temperature and gas pressure in cylindrical cells during thermal runaway, J. Power Sources (2024), https://doi.org/10.1016/j.jpowsour.2024.235147.

[19] D. Li, L. Wang, C. Duan, Q. Li, K. Wang, Temperature prediction of lithium-ion batteries based on electrochemical impedance spectrum: a review, Int. J. Energy Res. 46 (2022) 10372–10388, https://doi.org/10.1002/er.7905.

[20] L. Torres-Castro, A. Bates, N. Johnson, G. Quintana, L. Gray, Early detection of Li-ion battery thermal runaway using commercial diagnostic technologies, J. Electrochem. Soc. (2024), https://doi.org/10.1149/1945-7111/ad2440.

[21] S. Bhoir, G. Thenaisie, C. Brivio, M. Paolone, Li-ion cells internal temperature estimation using medium-frequency measurements of impedance argument, J. Energy Storage (2024), https://doi.org/10.1016/j.est.2024.112754.

[22] J. Chen, C. Xu, Q. Wang, H. Wang, Y. Peng, J. Liu, J. Zhang, G. Zhang, L. Lu, X. Feng, The thermal-gas coupling mechanism of lithium iron phosphate batteries during thermal runaway, J. Power Sources (2025), https://doi.org/10.1016/j.jpowsour.2024.235728.

[23] S.-Y. Li, S. Zhou, S. Zhao, T. Jin, M. Zhong, Z. Cen, P. Gao, W.-Y. Yan, M. Ling, Room temperature resistive hydrogen sensor for early safety warning of Li-ion batteries, Chemosensors (2023), https://doi.org/10.3390/chemosensors11060344.

[24] Y. Qian, Y. Zhao, Z. Li, Q. Wang, Y. Zhao, Gas detection technology for thermal runaway of lithium-ion batteries, Front. Physiol. (2025), https://doi.org/10.3389/fphy.2025.1615872.

[25] Z. Teng, C. Lv, Detection toward early-stage thermal runaway gases of Li-ion battery by semiconductor sensor, Front. Chem. 13 (2025), https://doi.org/10.3389/fchem.2025.1586903.

[26] Y. Jin, Z. Zheng, D. Wei, X. Jiang, H. Lu, L. Sun, F. Tao, D. Guo, Y. Liu, J. Gao, Y. Cui, Detection of micro-scale Li dendrite via H2 gas capture for early safety warning, Joule 4 (8) (2020) 1714–1729, https://doi.org/10.1016/j.joule.2020.05.016.

[27] M. Zhang, Z. He, W. Cheng, X. Li, X. Zan, Y. Bao, H. Gu, K. Homewood, Y. Gao, S. Zhang, Z. Wang, M. Lei, X. Xia, A room-temperature MEMS hydrogen sensor for lithium ion battery gas detecting based on Pt-modified Nb doped TiO2 nanosheets, Int. J. Hydrogen Energy (2024), https://doi.org/10.1016/j.ijhydene.2024.05.388.

[28] H. Cui, H. Wu, D. He, Shouxiao, Noble metal (Pd, Pt)-functionalized WSe2 monolayer for adsorbing and sensing thermal runaway gases in LIBs: a first-principles investigation, Environ. Res. (2025) 120847, https://doi.org/10.1016/j.envres.2025.120847.

[29] W. Hou, Q. Wang, Z. Li, N. Lyu, W. Zhong, Y. Jin, T. Liang, R. Wei, Hydrogen sensors of Ce-doped MoS2 with anti-humidity for early warning thermal runaway in lithium-ion batteries, Sens. Actuators B (2025), https://doi.org/10.1016/j.snb.2024.136988.

[30] O. Lupan, N. Magariu, D. Santos-Carballal, N. Ababii, J. Offermann, P. Pooker, S. Hansen, L. Siebert, N.H. de Leeuw, R. Adelung, Development of 2-in-1 sensors for the safety assessment of lithium-ion batteries via early detection of vapors produced by electrolyte solvents, ACS Appl. Mater. Interfaces 15 (22) (2023) 27340–27356, https://doi.org/10.1021/acsami.3c03564.

[31] T. Zheng, M. Muneeswara, H. Bao, J. Huang, L. Zhang, D.S. Hall, S.T. Boles, W. Jin, Gas evolution in Li-ion rechargeable batteries: a review on operando sensing technologies, gassing mechanisms, and emerging trends, ChemElectroChem 11 (15) (2024) e202400065, https://doi.org/10.1002/celc.202400065.

[32] Y.-X. Wang, B. Liu, B.-H. Liu, Y. Zhang, Oxygen-assisted recoverable hydrogen sensor based on sensing gate field effect transistor with ppb-level detection ability, Rare Metals 44 (2) (2025) 1160–1169, https://doi.org/10.1007/s12598-024-02976-3.

[33] Y. Huang, Y. Zhou, Y. Liu, J. Chen, X. Wei, J. Cao, SnO2/carbon nanotube floating-gate field-effect transistor gas sensor for ppb-level CO detection, ACS Appl. Nano Mater. 7 (14) (2024) 16119–16126, https://doi.org/10.1021/acsanm.4c01988.

[34] J. Peng, X. Zhao, J. Ma, D. Meng, J. Zhu, J. Zhang, S. Yan, K. Zhang, Z. Han, Enhancing lithium-ion battery monitoring: a critical review of diverse sensing approaches, eTransportation 22 (2024) 100360, https://doi.org/10.1016/j.etran.2024.100360.

[35] J. Jeong, J.-W. Lee, J. Lee, K. Shin, H.-S. Lee, W. Lee, Highly stable and reversible hydrogen sensors using Pd-coated SnO2 nanorods and an electrode–substrate interface as a parallel conduction channel, Sens. Actuators B 394 (2023) 134350, https://doi.org/10.1016/j.snb.2023.134350.

[36] Y. Zhou, Y. Ding, Y. Chen, Y. Shen, Z. Wang, X. Li, J. Xu, X. Huang, Thermal degradation of lithium-ion battery cathodes: a machine learning prediction of stability and safety, Energy Mater. 5 (7) (2025), https://doi.org/10.20517/energymater.2024.200.

[37] L. Huang, G. Xu, X. Du, J. Li, B. Xie, H. Liu, P. Han, S. Dong, G. Cui, L. Chen, Uncovering LiH triggered thermal runaway mechanism of a high-energy LiNi(0.5) Co(0.2) Mn(0.3) O(2) /Graphite pouch cell, Adv. Sci. 8 (14) (2021) e2100676, https://doi.org/10.1002/advs.202100676.

[38] X. Liu, L. Yin, D. Ren, L. Wang, Y. Ren, W. Xu, S. Lapidus, H. Wang, X. He, Z. Chen, G.L. Xu, M. Ouyang, K. Amine, In situ observation of thermal-driven degradation and safety concerns of lithiated graphite anode, Nat. Commun. 12 (1) (2021) 4235, https://doi.org/10.1038/s41467-021-24404-1.

[39] J. Lin, H.N. Chu, C.W. Monroe, D.A. Howey, Anisotropic thermal characterisation of large-format lithium-ion pouch cells**, Batteries Supercaps 5 (5) (2022), https://doi.org/10.1002/batt.202100401.

[40] C. Li, H. Wang, C. Shi, Y. Wang, Y. Li, M. Ouyang, A fitting method to characterize the gaseous venting behavior of lithium–ion batteries in a sealed chamber during thermal runaway, Energies 16 (23) (2023), https://doi.org/10.3390/en16237874.

[41] C. Li, H. Wang, Y. Li, M. Ouyang, A case study on gas venting events in NCM523 batteries during thermal runaway under different pressures in a sealed chamber, World Electric Veh. J. 16 (4) (2025), https://doi.org/10.3390/wevj16040189.

[42] J. Kim, A. Mallarapu, D. Finegan, S. Santhanagopalan, Modeling cell venting and gas-phase reactions in 18650 lithium ion batteries during thermal runaway, J. Power Sources 489 (2021), https://doi.org/10.1016/j.jpowsour.2021.229496.

[43] M. Kim, A.F. Ghoniem, J. Hong, Primary exothermic reaction pathways between solid electrolyte interphases and electrolytes during the onset of thermal runaway in lithium-ion batteries, Energy Storage Mater. 81 (2025), https://doi.org/10.1016/j.ensm.2025.104537.

[44] M. Kim, J. Jeon, J. Hong, Reaction mechanism study and modeling of thermal runaway inside a high nickel-based lithium-ion battery through component combination analysis, Chem. Eng. J. 471 (2023), https://doi.org/10.1016/j.cej.2023.144434.

[45] C. Orendorff, The role of separators in lithium-ion cell safety, Interface-Electrochem. Soc. 21 (2012) 61, https://doi.org/10.1149/2.F07122if.

[46] L. Schmidt, K. Hankins, L. Blaubaum, M. Gerasimov, U. Krewer, High temperature in situ gas analysis for identifying degradation mechanisms of lithium-ion batteries, Chem. Sci. 16 (12) (2025) 5118–5128, https://doi.org/10.1039/d4sc08105f.

[47] H. Shen, H. Wang, M. Li, C. Li, Y. Zhang, Y. Li, X. Yang, X. Feng, M. Ouyang, Thermal runaway characteristics and gas composition analysis of lithium-ion batteries with different LFP and NCM cathode materials under inert atmosphere, Electronics 12 (7) (2023), https://doi.org/10.3390/electronics12071603.

[48] J.-S. Shin, C.-H. Han, U.-H. Jung, S.-I. Lee, H.-J. Kim, K. Kim, Effect of Li2CO3 additive on gas generation in lithium-ion batteries, J. Power Sources 109 (1) (2002) 47–52, https://doi.org/10.1016/S0378-7753(02)00039-3.

[49] K. Wang, D. Wu, C. Chang, J. Zhang, D. Ouyang, X. Qian, Charging rate effect on overcharge-induced thermal runaway characteristics and gas venting behaviors for commercial lithium iron phosphate batteries, J. Clean. Prod. 434 (2024) 139992, https://doi.org/10.1016/j.jclepro.2023.139992.

[50] J. Ye, J. Huang, J. Kuang, J. Tang, C. Liu, R. Li, G. Tan, Data-driven methods for early warning of battery thermal runaway: a review of multi-signal fusion and machine learning approaches, J. Energy Storage 133 (2025) 118043, https://doi.org/10.1016/j.est.2025.118043.

[51] D. Kong, H. Lv, P. Ping, G. Wang, A review of early warning methods of thermal runaway of lithium ion batteries, J. Energy Storage 64 (2023) 107073, https://doi.org/10.1016/j.est.2023.107073.

[52] S. Yin, J. Liu, B. Cong, Review of thermal runaway monitoring, warning and protection technologies for lithium-ion batteries, Processes 11 (8) (2023) 2345.

[53] X. Zhang, S. Chen, J. Zhu, Y. Gao, A critical review of thermal runaway prediction and early-warning methods for lithium-ion batteries, Energy Mater. Adv. 4 (2023) 0008, https://doi.org/10.34133/energymatadv.0008.

[54] Z. Yang, Z. Gu, Q. Tao, J. Bao, H. Li, S. Wang, Early warning technology for common characteristic resistances of lithium-ion batteries with thermal runaway, Chem. Commun. 60 (1) (2024) 87–90, https://doi.org/10.1039/D3CC05086F.

[55] W. Mei, Z. Liu, C. Wang, C. Wu, Y. Liu, P. Liu, X. Xia, X. Xue, X. Han, J. Sun, G. Xiao, H.Y. Tam, J. Albert, Q. Wang, T. Guo, Operando monitoring of thermal runaway in commercial lithium-ion cells via advanced lab-on-fiber technologies, Nat. Commun. 14 (1) (2023) 5251, https://doi.org/10.1038/s41467-023-40995-3.

[56] S. Chen, X. Wei, G. Zhang, X. Wang, X. Feng, H. Dai, M. Ouyang, Mechanical strain signal based early warning for failure of different prismatic lithium-ion batteries, J. Power Sources 580 (2023) 233397, https://doi.org/10.1016/j.jpowsour.2023.233397.

[57] X. Gu, Y. Shang, J. Li, Y. Zhu, X. Tao, H. Geng, Z. Zhang, C. Zhang, Early warning of thermal runaway based on state of safety for lithium-ion batteries, Commun. Eng. 4 (1) (2025) 106, https://doi.org/10.1038/s44172-025-00442-1.

[58] Z. Li, M. Jiao, K. Chen, Y. Gao, Y. Gao, C. Lian, J. Zhang, F. Xuan, A self-decoupling multimodal sensor for enhanced early warning of lithium-ion battery thermal runaway, Research (Wash. D. C.) 9 (2026) 1120, https://doi.org/10.34133/research.1120.

[59] B. Li, M.H. Parekh, R.A. Adams, T.E. Adams, C.T. Love, V.G. Pol, V. Tomar, Lithium-ion battery thermal safety by early internal detection, prediction and prevention, Sci. Rep. 9 (1) (2019) 13255, https://doi.org/10.1038/s41598-019-49616-w.

[60] M.H. Parekh, B. Li, M. Palanisamy, T.E. Adams, V. Tomar, V.G. Pol, In situ thermal runaway detection in lithium-ion batteries with an integrated internal sensor, ACS Appl. Energy Mater. 3 (8) (2020) 7997–8008, https://doi.org/10.1021/acsaem.0c01392.

[61] X. Chen, L. Gan, X. Guo, Optical fiber-based gas sensing for early warning of thermal runaway in lithium-ion batteries, Adv. Sensor Res. 2 (12) (2023) 2300055, https://doi.org/10.1002/adsr.202300055.

Glossary

Δt_{TR} *(Warning Interval): The time interval between the first detection of hydrogen gas and the onset of thermal runaway; a key predictive metric.:*
Δt_{max}*: The time interval between the initial detection of* H_2 *and its peak concentration, representing the degree of temporal compression in hydrogen evolution with increasing heating rate.:*
$[H_2]_{peak}$*: The peak concentration of hydrogen gas during thermal events, indicating the intensity of gas generation.:*
$d[H_2]/dt$*: The rate of increase of hydrogen concentration over time; a rapid rise signals heightened runaway risk.:*
T_{cell}*: The real-time measured surface temperature of the cell, used to provide thermal context during the experiment.:*
T_{TR}*: The cell surface temperature at the onset of thermal runaway, used to correlate gas evolution behavior with thermal transition.:*